doi:10.20944/preprints201907.0183.v1

Peer-reviewed version available at *Catalysts* **2019**, *9*, 708; doi:10.3390/catal9090708

Article

Immobilized rGO/TiO₂ photocatalyst for decontamination of water

Radek Zouzelka, Monika Remzova, Jan Plsek, Libor Brabec and Jiri Rathousky *

J. Heyrovsky Institute of Physical Chemistry of the CAS, Dolejskova 3, Prague 18223, Czech Republic
* Correspondence: jiri.rathouskyh-inst.cas.cz

Abstract: The preparation of immobilized graphene–based photocatalyst layers is highly desired for environmental applications. In this study, the preparation of an immobilized reduced graphene oxide (rGO)/TiO_2 composite by electrophoretic deposition (EPD) was optimized. It enabled quantitative deposition without sintering and without the use of any dispersive additive. The presence of rGO had beneficial effects on the photocatalytic degradation of 4-chlorophenol in an aqueous solution. A marked increase in the photocatalytic degradation rate was observed, even at very low concentrations of rGO. Compared with the TiO_2 and GO/TiO_2 reference layers, use of the rGO/TiO_2 composite (0.5 wt% of rGO) increased the first-order reaction rate constant by about 70%. This enhanced performance was due to the increased formation of hydroxyl radicals that attacked the 4-chlorophenol molecules. The direct charge transfer mechanism had only limited effect on the degradation. Thus, EPD-prepared rGO/TiO_2 layers appear to be suitable for environmental application.

Keywords: electrophoretic deposition; photocatalysis; TiO_2; reduced graphene oxide; water purification

1. Introduction

Graphene-based nanomaterials possess unique properties that can be applied to environmental remediation [1–5]. The interest in these nanomaterials originates from graphene's unique physicochemical properties, notably its exceptionally high surface area, electron and thermal mobility, and mechanical strength. One of the most popular approaches for preparing graphene-based nanomaterials involves the use of graphene oxide (GO) because of its lower production costs. GO is an oxidized form of graphene, showing a high density of oxygen functional groups (carboxyl, hydroxyl, carbonyl, and epoxy) in the carbon lattice. However, the oxidation of graphite to GO introduces defects into the carbon structure that results in significantly altered physicochemical properties.

By the reduction of GO, a large fraction of its oxygen content can be removed, which leads to a substantial change in its physico-chemical properties. The formed reduced graphene oxide (rGO) possesses enhanced electronic (higher mobility of electrons), optical and surface properties (decreased wettability) [4]. Moreover, reduction also results in an altered chemical structure, with carbon vacancies, residual oxygen content, clustered pentagons and heptagons carbon structures. Thus, the complete reduction of GO is challenging. Despite these defects, the physicochemical properties of rGO represent a partial restoration that is closer to pristine graphene than GO.

Restoring the physicochemical properties of graphene is vital for the production of graphene-based composite materials. However, the improved performance of graphene-based composites often relies on synergistic interactions between the rGO and the materials attached to its surface. Therefore, the quality of the graphene-based materials used will have an important impact on the performance of the final nanocomposite.

In the environmental field, graphene-based nanocomposites have been used to develop novel adsorbents [8] and photocatalysts [2,7,8]. Adsorption is a fast, inexpensive, and effective method for the removal of contaminants from aquatic environments [9]. It is based on physicochemical interactions between the adsorbent and contaminant. Although rGO-based adsorbents can remove contaminants from water, this technique does not degrade the compounds, which require further disposal. Thus, for the complete mineralization of organic pollutants, photocatalytic treatment is often more suitable [10].

Composite graphene-based photocatalysts have been mostly tested in the form of suspensions, [1,11] which is favorable from the point of view of the mass transport of reactants and degradation products. However, for environmental remediation and clean-up applications, immobilized photocatalysts are often preferable for several reasons: (i) they do not require complicated separation or filtration steps, (ii) a thin layer deposited on a suitable substrate can be easily incorporated into continuous flow systems, and, last but not least, (iii) the aggregation, or even agglomeration, of particles can be prevented. Despite this, to the best of our knowledge, no study has reported the preparation of an immobilized rGO-based photocatalyst for the removal of environmental pollutants.

In this study, we optimized the suspension and process parameters of the electrophoretic deposition (EPD) process to prepare an rGO-based photocatalyst immobilized on stainless-steel substrates for the photocatalytic degradation of 4-chlorophenol. Our criteria were rGO/TiO_2 layer homogeneity, good mechanical stability in aqueous media, strong adhesion to the substrate, and, in particular, high photocatalytic activity. In the degradation of 4-chlorophenol, our nanocomposite was much more effective than pristine TiO_2.

2. Results

2.1. Preparation of layers by EPD

In order to quantitatively prepare rGO/TiO_2 photocatalytic layers of desired mass without using additives (e.g. binders, surfactants), EPD should be carried out under highly specific conditions. Using novel mixtures of organic solvents and strong electric field, we found that quantitative deposition was feasible. Furthermore, the layers prepared were ready for photocatalytic testing immediately after EPD and fast volatile solvent evaporation. Neither heating for drying nor calcination for layer consolidation was necessary because the deposited composite did not contain any additional impurity and was mechanically stable when immersed in aqueous media.

Using our method, all of the particles dispersed in an organic solvent mixture were completely deposited on the substrate used. We identified tetrahydrofuran (THF) as the most suitable solvent for rGO/TiO_2 deposition because of its low toxicity, sufficient volatility and suitable electric properties (especially low relative permittivity and low conductivity). Particles of TiO_2, dispersed in ethanol and injected into THF, and of rGO, dispersed in 2-propanol and injected into THF, exhibited positive and negative charges, respectively. However, in the presence of positively charged TiO_2 particles, rGO did not migrate to the anode because the positive charge of TiO_2 prevailed and, consequently, the composite was deposited on the cathode. Particle settling was negligible due to their low concentration (< 0.5 g L^{-1}) and small particle size. The low conductivity of THF enabled the application of high electric field strength (300 V cm^{-1}). The initial electric current did not exceed 30 μA and during EPD it decreased approximately twofold due to the resistance of the deposited layer. The experimental conditions neither influenced the physico-chemical properties of deposited particles nor were detrimental to the layer stability.

2.2. Properties of graphene materials

The morphological properties of the graphene materials, GO and rGO, were quite different. The starting graphene oxide powder GO was characterized by a very large surface area of ca. 1800 m^2 g^{-1} (Figure 1c), which is in reasonable agreement with the theoretical surface area of graphene sheets [12]. The two-dimensional character of this material was confirmed by FE-SEM (Figure 1a) and HRTEM (Figure 2b). The isotherms did not exhibit any stepwise character, which was clearly due to the heterogeneous structure of the surface (due to the presence of defects and various oxygen functional groups). The reduction of GO in a stream of hydrogen at 400 ^{o}C brought about drastic morphological changes. The BET surface area of the rGO sample decreased to 108 m^2 g^{-1}, the range

Peer-reviewed version available at *Catalysts* **2019**, *9*, 708; doi:10.3390/catal9090708

of the validity of the BET equation being very narrow, only from 0.05 to 0.15 P/P_0. That this material is to some extent microporous was revealed by the Broekhoff-de Boer t-plot. The micropore volume determined by the back-extrapolation of the linear multilayer section was about 0.012 $cm^3\ g^{-1}$. Assuming that this linear section represents unrestricted multilayer adsorption on the external surface, its approximate area was around 83 $m^2\ g^{-1}$. Thus, it is reasonable to hypothesize that the change in the morphology may have been due to the sintering of carbon particles or the formation of holes because of the high-temperature reduction process.

Thermogravimetric analysis (TGA) showed that rGO had much higher thermal stability than GO due to its lower content of oxygenated functional groups. In GO (Figure 2b), a slight decrease in mass (8%) occurred between 100 and 200 °C, which can be associated with the removal of hydroxyls and adsorbed water. After this slight reduction, significant mass loss (25%) followed, indicating the exothermal release of CO and CO_2 from the most labile functional groups. At temperatures below 800 °C, the total mass loss was about 80%. However, in contrast to GO, rGO showed very high thermal stability with a total mass loss of only 10% at temperatures below 800 °C, corresponding to the low content of oxygen functional groups in its structure (Figure 2b).

FTIR spectroscopy showed that the spectra of the GO and rGO layers differed considerably. The GO spectrum indicated the presence of oxygen-containing functional groups together with sorbed water (Figure 1d), in accordance with the published data [13,14]. The bands at 1375 and 1090 cm^{-1} correspond to deformation vibrations of sorbed water while the broad bands at 1900–2300 and 3100–3600 cm^{-1} are associated with bridging hydroxyls (O–H), obviously overlapped by the sorbed water molecules [15]. The absorption bands at 1720 and 1620 cm^{-1} show C=O stretching of carbonyl groups, which are adjacent to the hexagonal graphene lattice. The overlapped bands at 1420 and 950 cm^{-1} are attributed to deformations of carboxyl O–H groups, while the peak centered at 1220 cm^{-1} is assigned to C–O carboxylic stretch. The absorption band with strong intensity at 1042 cm^{-1} can be associated with alkoxy functional groups (C–O). The band at 1267 cm^{-1} can be attributed to epoxy ring stretch. The band at 870 cm^{-1} can be assigned either to ether symmetric C–O–C or epoxide symmetric C–O–C ring deformation vibrations. Moreover, the GO structure was represented by out of plane vibrations of aromatic ring at 655 cm^{-1} as well as vibrations of alkyl groups (C–H) at higher frequencies of 2850, 2920 and 2975 cm^{-1}. After GO reduction, the FTIR spectra changed significantly, reflecting the elimination of the oxygen functional groups. Absorption at 3100−3600 cm^{-1} (bridging hydroxyls) decreased noticeably with the diminishing intensity of the 1620 cm^{-1} and 1375 cm^{-1} absorption bands, which was due to the substantial removal of sorbed water. Furthermore, carboxyl (950 and 1420 cm^{-1}), alkoxy (1042 cm^{-1}) and ether/epoxide (870 cm^{-1}) bands were substantially reduced. Contrary, the new absorption bands at 1580 cm−1 corresponding to C–C vibrations and at 742 cm^{-1} corresponding to vibration of sp^2 C–H aromatic bond appeared. This suggests the restoration of the conjugated aromatic graphene structure. However, the distinguishable absorption band associated with C–O carboxylic groups (1220 cm^{-1}) at the edges of the planes remained as well as the carbonyl groups (1720 cm^{-1}). Overall, the data obtained by IR spectroscopy shows that reduction of GO under hydrogen atmosphere at high temperature resulted in substantial decrease of the concentration of a majority of oxygenated groups, while that of carboxylic groups appeared to be considerably less prominent.

XPS verified the FTIR data by confirming the elemental composition before and after reduction. Both C1s (Figure 1e, Table 1) and O1s (Figure 1f, Table 2) spectra confirmed the substantial reduction of oxygen functional groups of GO sample. The O/C ratio before and after reduction was 0.53 and 0.19, respectively, which means that 60% of oxygen groups were reduced. Deconvolution of O1s spectra resulted in three peaks centered at 531.3, 533.0 and 535.3 eV assigned to carbonyl, hydroxyls and sorbed water molecules [16]. The high-resolution C1s spectra clearly show the difference

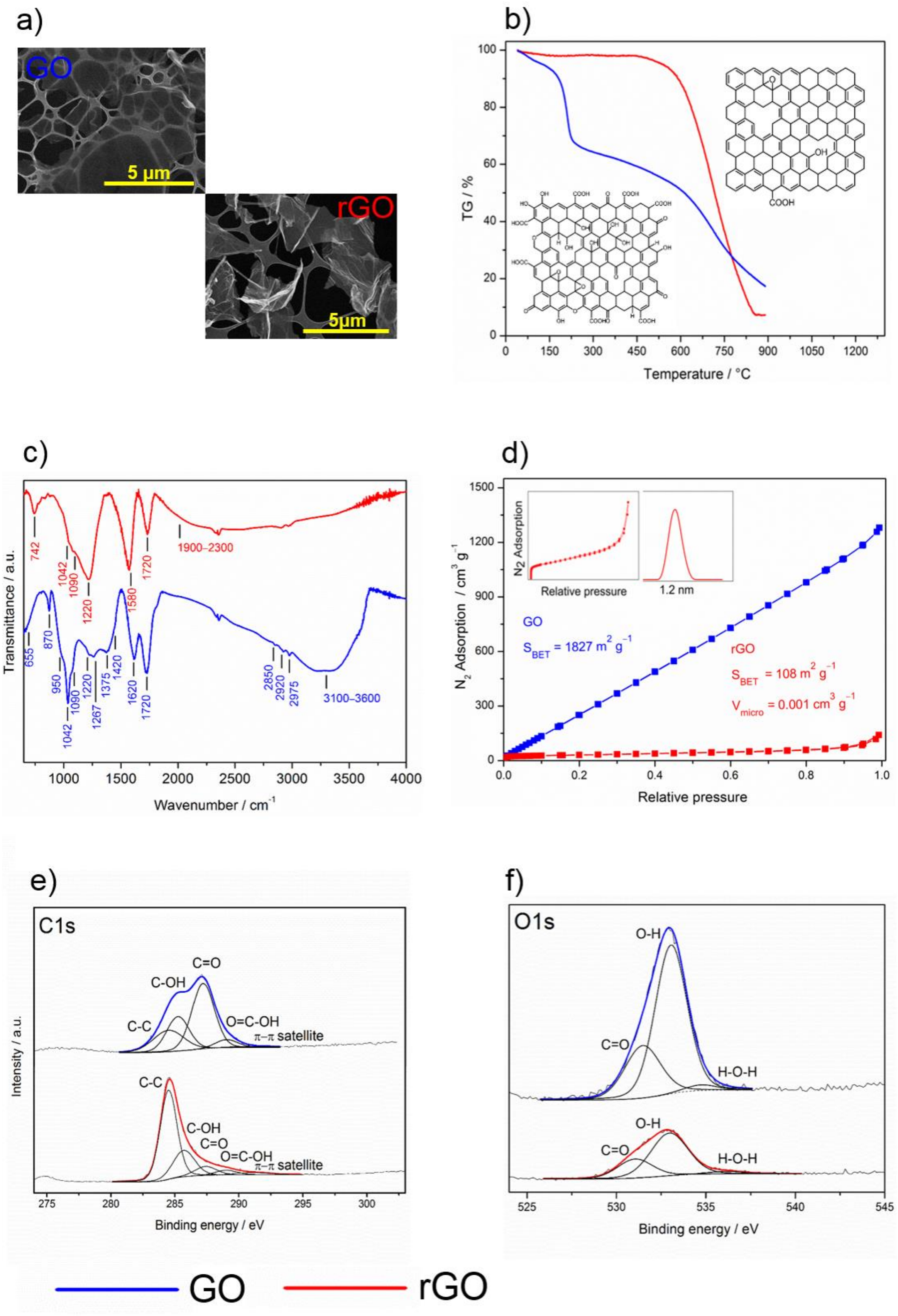

Figure 1. Physico-chemical properties of graphene oxide (GO, blue) and reduced graphene oxide (rGO, red). (a) SEM images, (b) thermogravimetry, (c) FTIR spectra, (d) physical sorption of nitrogen, (e) C1s and (f) O1s XPS spectra.

Preprints (www.preprints.org) | NOT PEER-REVIEWED | Posted: 15 July 2019 doi:10.20944/preprints201907.0183.v1

Peer-reviewed version available at Catalysts 2019, 9, 708; doi:10.3390/catal9090708

between GO and its reduced form. In the GO lattice structure, the carbon atoms were bonded either to the carbon forming C–C conjugation (284.5) or to the oxygen forming carboxyl (288.6 eV), carbonyl (287.4 eV) and hydroxyl (285.6 eV) functional groups. These assignments are in qualitative agreement with those in literature even though there is certain vagueness in exact binding energy value determination for individual components [16–21]. For both GO and rGO, the asymmetry of the C–C peak was observed, which was probably related to the screening of the core holes left by photoelectrons. Increase of aromatic sp^2 (284.5 eV) in C1s spectrum after reduction indicates that the delocalized π conjugations in rGO were significantly restored.

Table 1. Amount of various oxygenated groups before and after reduction of GO calculated from the C1s XPS spectra.

Sample	C–C / %	C–OH / %	C=O / %	O=C–OH / %
GO	22.7	24.6	46.8	5.8
rGO	63.5	23.9	8.2	4.3
rGO/TiO_2	66.7	19.4	8.2	5.6

Table 2. Amount of various oxygenated groups before and after reduction of GO calculated from the O1s XPS spectra.

Sample	C=O / %	C–OH / %	H–O–H / %
GO	27.6	69.8	2.6
rGO	28.5	67.7	3.8
rGO/TiO_2	26.6	66.5	6.9

2.3. Properties of rGO/TiO$_2$ composite layers

The survey XPS spectra of the rGO/TiO_2 composite layer shows the presence of carbon, titanium and oxygen atoms while no other elements were identified on the surface at the detection limit. The high-resolution C1s spectra showed similar level of reduction as bare rGO (compare Figure 1e and Figure 2d), with exception of the peak assigned to carboxyl groups which seem to be more pronounced. This confirmed the data obtained by infrared spectroscopy. Ti2p XPS spectrum (Figure 2c) with peak Ti 2p$_{3/2}$ centered at 459.4 eV and spin-orbit-splitting of 5.6 eV documents presence of fully oxygen coordinated Ti^{4+} species.

SEM and HRTEM images of composite layers are shown in Figure 2a and Figure 2b, respectively. The SEM image shows that the rGO sheets are homogeneously distributed within the whole volume of the layer preferentially parallel with the steel substrate. The HRTEM image proves the heterojunction between TiO_2 particles and rGO sheets. In the inset to the HRTEM image the contact of an individual TiO_2 crystal with a single rGO is shown.

The diffuse reflectance spectra of the rGO/TiO_2 showed absorption edges below 400 nm. The spectra were plotted the spectra using the Kubelka–Munk F(R) function expressed in Equation (1)

$$\mathrm{F(R)} = \frac{(1-\mathrm{R})^2}{2\mathrm{R}} = \frac{\alpha}{\mathrm{s}}, \tag{1}$$

where *R*, *α* and *s* are the diffuse reflectance, the absorption and scattering coefficients [22]. The optical band gap energy was determined using Equation (2)

$$(\mathrm{F(R)\ h\nu})^{1/\mathrm{n}} \sim (\mathrm{h\nu} - \mathrm{E_g}), \tag{2}$$

where *F(R)*, *h*, *ν*, *E$_g$* and *n* are the Kubelka–Munk function, the Planck constant, the oscillation frequency, the band gap energy and the constant relating to the mode of transition. The minimal-energy state in the conduction band and the maximal-energy state in the valence band are each

Peer-reviewed version available at Catalysts 2019, 9, 708; doi:10.3390/catal9090708

characterized by a k-vector in the Brillouin zone [23]. Two types of band-to-band transitions are suggested. First, direct transitions, where the k-vectors are the same and the participation of a phonon is not required to conserve momentum. Second, indirect transitions, where at least one phonon participates in the absorption or emission of a photon to conserve momentum. The constant n equals 1/2 for the allowed direct, 3/2 for the forbidden direct or 2 for the allowed indirect transitions. We checked the linearity of the plots of $(F(R)\ h\nu)^{1/n}$ against $h\nu$ using n=1/2 (allowed direct) to assess the mode of the transition of a given crystal. More details are provided in the review by Ohtani [23]. Using the Tauc plot, the optical band gap energies E_g for the TiO_2 and rGO/TiO_2 layers were calculated [24]. The absorption data were fitted according to Equation 1 for allowed direct band gap transitions and satisfactory fit was obtained, giving E_g values of 3.20 and 3.25 for rGO/TiO_2 and TiO_2, respectively (Figure 2f).

2.4. Photocatalytic performance of rGO/TiO$_2$ layers

As a test reaction, we used the photocatalytic degradation of 4-chlorophenol because this compound is a common water pollutant that exhibits good chemical stability, undergoes negligible photolysis, and possesses relatively low adsorption on the photocatalyst surface.

First, the effect of the stability of the deposited layers on their photocatalytic performance was determined. Experiments showed that the layers deposited on the stainless steel surface exhibited very good adhesion, with no leaking of titania or carbonaceous particles during the photocatalytic tests. No particles were detected in the solution after the experiments.

Having determined the adhesion properties of the composite, we investigated the photocatalytic performance of the GO/TiO_2 and TiO_2 layers. As they exhibited similar activities, the doping with GO did not produce any substantial improvement in photocatalytic activity. This performance is due to the physico-chemical properties of GO, which is an insulant with abundant oxygenated surface groups. This drawback was removed by the reduction of GO, which transformed the insulant GO into more or less highly conductive rGO.

The improved photocatalytic performance is shown in Figure 3a, in which the decrease in 4-chlorophenol concentration using rGO/TiO_2 was statistically significantly much faster. The first-order reaction rate constant for rGO/TiO_2 was 0.0053 min^{-1}, which was 70% higher than that for GO/TiO_2 or TiO_2. When reused, the layers showed no deterioration in photocatalytic performance, which is very important from the application point of view (Figure 3b).

Generally, a photocatalytic process involves two different mechanisms: a direct transfer of charge carriers and an attack by radicals, especially by hydroxyl ones. Depending on the reaction conditions, these mechanisms may act separately or jointly.

To explain the mechanism of 4-chlorophenol photocatalytic degradation, in our previous studies, we employed experimental and theoretical (DFT) approaches. Our results therein showed that the hydroxylation and opening of the aromatic ring can occur in parallel with the release of the hydroperoxyl and hydroxyl radicals [6,25]. The restored OH radical can either further oxidize the primary ring opening product or attack another molecule of 4-chlorophenol. These DFT results were in good agreement with the photocatalytic degradation experiments conducted using both ZnO and TiO_2 photocatalysts [6,25]. According to the parallel mechanism, the products of 4-chlorophenol degradation are the experimentally-identified aromatics hydroquinone and benzoquinone, as well as various ring-opening compounds formed under the restoration of OH radical (Figure 4a).

In this study, the enhanced performance of the rGO/TiO_2 photocatalyst can be explained by an increased formation of radicals owing to a better separation of charge-carriers. This phenomenon can be caused by the downward bending of the TiO_2 conduction band due to the presence of rGO, which can suppress the charge-carrier recombination. The recombination can be further suppressed by the high mobility of electrons over the graphene surface. The freed oxidative holes can react either directly with the pollutant molecules or indirectly through the OH radicals, which are strong oxidants.

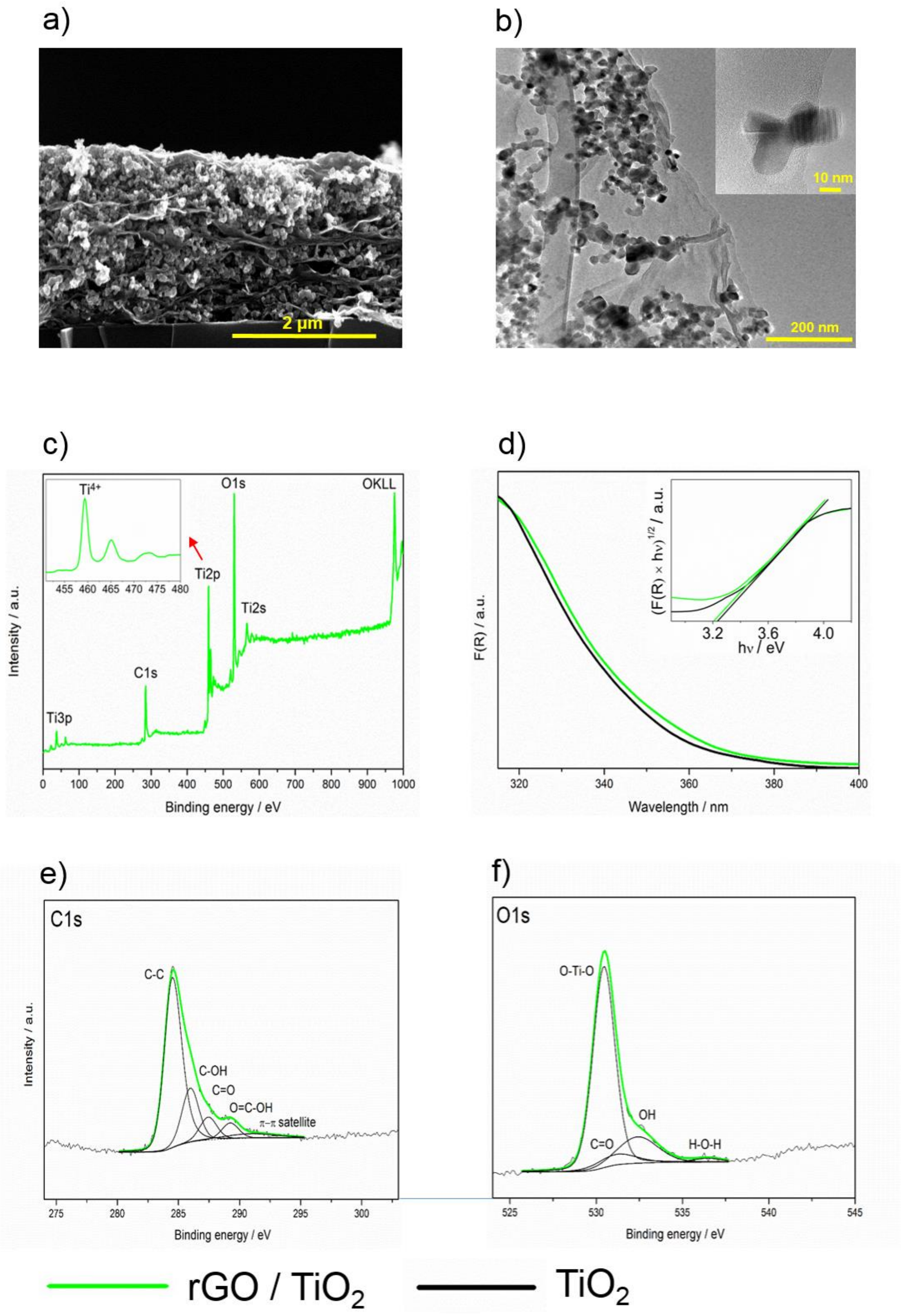

Figure 2. a) SEM cross-section image of a composite layer containing TiO_2 and rGO, b) HRTEM image of the composite, c) Survey XPS spectrum of the rGO/TiO_2 composite layer, (d) UV/vis spectra of the rGO/TiO_2 and TiO_2 layers (e) C1s and (f) O1s spectra rGO/TiO_2 composite layer.

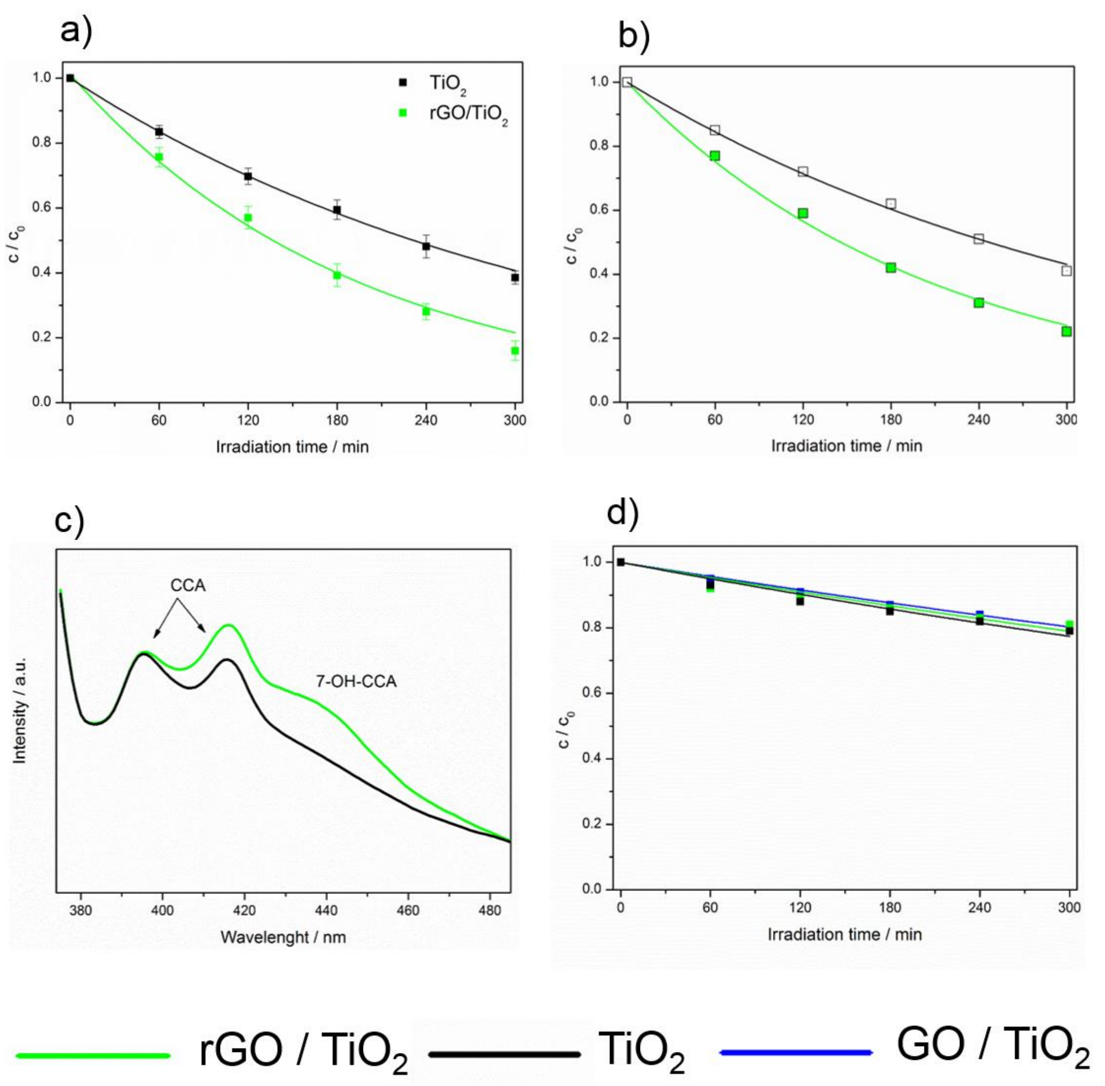

Figure 3. a) Course of the photocatalytic degradation of 4-chlorophenol on TiO2 and rGO/TiO2 photocatalysts, b) Reusability of TiO2 and rGO/TiO2 photocatalysts, c) Fluorescence spectra of 7-OH-coumarin-3-carboxylic acid after irradiation of TiO_2 and rGO/TiO_2 with 365 nm light for 30 seconds, d) Effect of OH radical scavenger (2-propanol) on the course of the 4-chlorophenol photocatalytic degradation on TiO_2, GO/TiO_2 and rGO/TiO_2.

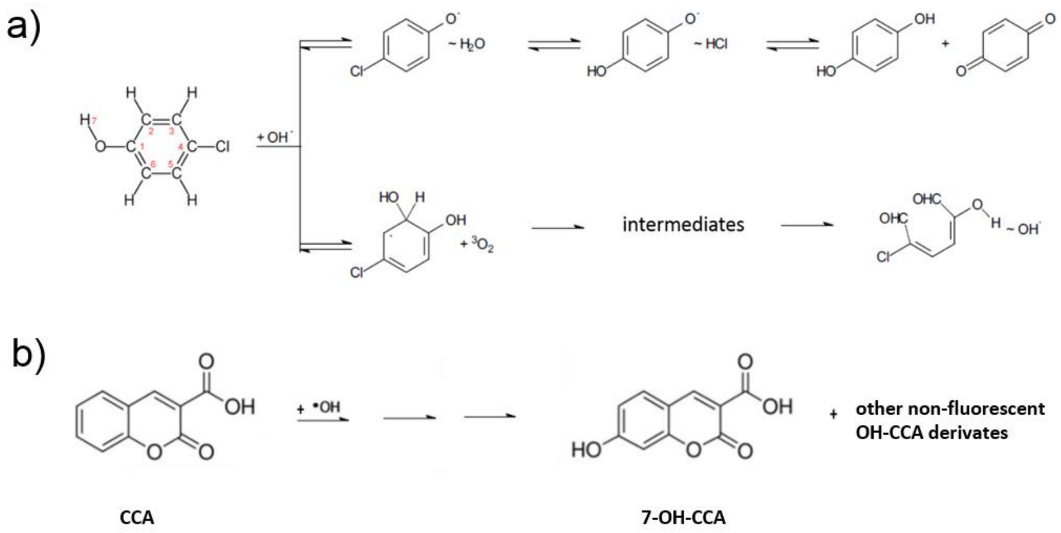

Figure 4. a) Simplified scheme of the photocatalytic 4-chlorophenol degradation b) Reaction of OH radical with coumarin 3-carboxy acid to form fluorescent molecule 7-hydroxy coumarin 3-carboxy acid.

Due to the high reactivity and short lifetime in water of OH radicals, their direct detection is very difficult. Thus, for their indirect detection, a fluorescence spectroscopy was employed using coumarin-3-carboxylic acid. After the UV irradiation of TiO_2, this acid reacts with OH radicals to produce 7-OH-coumarin-3-carboxy acid (Figure 4b), emitting strong fluorescence at 442 nm. Compared with the TiO_2 sample, rGO/TiO_2 exhibited higher fluorescence intensity (Figure 3c).

Additional experiments performed to confirm the predominant mechanism of 4-CP degradation on the doped and undoped TiO_2 layers showed that indirect action through radicals played the major role. However, its predominance only became clear when 2-propanol was used as a radical scavenger. Due to the similar rate constants of the reaction of the hydroxyl radical with 2-propanol [26] and with 4-chlorophenol [27], a 1000fold excess of 2-propanol would practically stop the degradation of 4-chlorophenol if only OH-attack is responsible for it. However, as can be seen in Figure 3d, the photocatalytic degradation of 4-chlorophenol only slowed down, 6.7 times for rGO/TiO_2, 4.2 times for GO/TiO_2 and 3.6 times for pristine TiO_2 layer (pseudo first order reaction rate constants of 0.00079 ± 0.00004, 0.00073 ± 0.00004 and 0.00085 ± 0.00005 min^{-1}, respectively), but continued. These similar rate constants suggest that direct charge transfer participated similarly in the photocatalytic degradation of 4-chlorophenol in each case and that the presence of the rGO dopant did not influence this mechanism. However, the presence of rGO did positively influence the photocatalytic degradation of 4-chlorophenol in the absence of 2-propanol (pseudo-first order rate constants of 0.0031 and 0.0053 min^{-1} for TiO_2 layers without and with rGO, respectively), which therefore is probably due to enhanced radical production.

3. Materials and Methods

Materials. The commercial 2 to 4 layered graphene oxide and Aeroxide TiO_2 P 25 were purchased from Cheaptubes.com and Evonik Industries, respectively. Organic solvents (p.a. purity) acetone, tetrahydrofuran, heptane, 2-propanol and ethanol were supplied by Penta, Czech Republic. Sheets of glossy stainless steel AISI 304 (25 × 50 × 1 mm^3) served as electrodes.

Preparation of rGO. The commercial GO sample was reduced in a stream of hydrogen (10 mL/min) at 400 °C for 8 hours to obtain reduced graphene oxide rGO used for the deposition of composite layers.

Preparation of rGO/TiO_2 composite layers. Prior EPD, electrodes were washed ultrasonically in deionized water and acetone. During EPD, the electric field was adjusted to 300 V cm^{-1} using DC power supply EV245 (Consort, Belgium). Polished stainless-steel plates served as the working (cathode) and counter electrode (anode). The distance between vertically placed electrodes was 11 mm. The deposition mixture was prepared by a two-step process. First titanium dioxide (2 or 4 g/L) and rGO (up to 0.4 g/L) were dispersed in ethanol or 2-propanol. Then a small volume (0.25 or 0.5 mL) of these dispersions was injected into tetrahydrofuran (10 mL). The titania loading on the support was between 0.03 and 2.5 mg cm^{-2}. 10 minutes of EPD process was found sufficient for the deposition of all dispersed particles.

Characterization. The elements present in titania, graphene oxide and reduced graphene oxide, as well as their chemical state were identified by X-ray photoelectron spectrometer (VG ESCA3 MkII) with a base pressure better than 10^{-9} mbar. For the excitation of the electrons, Al Kα radiation was used. The energy of electrons was analysed using a hemispherical analyser, which operated at constant pass energy of 20 eV. The XPS spectra were calibrated by setting C1s peak belonging to sp^2 component at the binding energy of 284.5 eV. The estimated error in binding energy determination was ±0.1 eV. The surface atomic content was accomplished assuming a homogenous distribution of atoms and Scofield photoionization cross-section. The crystallinity of titania powders was measured using a D5000 high-resolution X-ray diffractometer (Siemens) operated at 40 kV and 45 mA with Cu Kα radiation (λ = 1.5406 Å). The texture properties of powders and layers were determined by the analysis of adsorption isotherms of nitrogen or krypton at ca 77 K performed with a Micrometrics 3FLEX volumetric adsorption unit. The surface profile of layers was studied with a FE-SEM instrument Hitachi S-4800 and HRTEM instrument JEM-2100Plus. The optical properties of the layers were measured with a Lambda 950 UV-Vis-NIR spectrometer (Perkin Elmer) equipped with

Peer-reviewed version available at Catalysts 2019, 9, 708; doi:10.3390/catal9090708

Spectralon and gold integration spheres for diffuse reflectance measurements in the UV-Vis-NIR region, and with a Fourier transform infrared spectrophotometer Nicolet 6700. The thermogravimetric measurements were carried out in a flow of Ar at a temperature ramp of 10 K/min using a TGA-MS Netzsch STA449 apparatus.

Photocatalytic experiment. Before the photocatalytic experiments, the samples to be tested were cleaned overnight by UV light of a dominant wavelength of 365 nm with irradiation intensity of 2.0 mW cm^{-2} to decompose any residual organic matter on them. The 4-chlorophenol in aqueous solution (0.1 mmol L^{-1}) was photocatalytically degraded at 25 °C on TiO_2 and doped TiO_2 layers (TiO_2 mass of 0.5 mg, rGO mass of 0.025 mg, substrate area of 6 cm^2) in a 25 mL quartz cell. As the top of the liquid in the cell was open to air and the solution was intensively stirred, the concentration of dissolved oxygen was constant during the experiment. A Sylvania Lynx-S 11 W BLB lamp irradiated the layer surface with UV light (365 nm) at a low power density of 1.0 mW cm^{-2}. Prior to the photocatalytic experiments, the dissolved 4-chlorophenol was equilibrated with the photocatalyst surface for three hours. For each experiment, six aliquots each of 100 μL were taken from the solution in the reaction cell at regular time intervals and analyzed by high-performance liquid chromatography. The first-order reaction rate constants for the 4-chlorophenol degradation were calculated using a nonlinear regression fitting of the kinetic curves. In the mechanistic study the scavenger (2-propanol) was added at the very beginning of the experiment in a concentration of 10^{-1} M. For the detection of OH radicals formed during the irradiation of titanium dioxide and its composite containing rGO with 365 nm light, we employed a fluorescence spectroscopy (Fluorolog 3, Horiba). In this experiment, an aqueous 10^{-4} M solution of coumarin-3-carboxylic acid reacted with OH radicals to produce 7-OH-coumarin-3-carboxylic acid, which was excited at 365 nm and emitted a strong fluorescence at 442 nm. The photoluminescence (PL) spectra of the layers were measured using continuous PL wave of the 4th harmonic (266 nm) line of YAG:Nd laser and dispersed with a HR250 monochromator (Jobin-Yvon) coupled with UV-enhanced Intensified Charge Coupled Device (ICCD) (Roper). Under pulsed laser excitation, PL spectra were recorded in a pseudo CW mode with a continuous integration of the intensity in 300 ms corresponding to three full illumination pulses.

Data analysis and statistics. The photocatalytic experiments were done in three replicates. Significant differences between compared samples were determined by using Student's *t* test where *p* values were used as the threshold for statistical significance. Normality of the data and homogeneity of variance were tested using the Pearson's chi-squared test of goodness of fit and the Levene's test (Statistica software, StatSoft CR), respectively. The tests showed that the data fulfilled assumptions for the parametric statistics applied (i.e., normality of the data and homogeneity of variance).

4. Conclusions

We have shown that our optimized EPD technique enables the fast and simple preparation of an immobilized rGO/TiO_2 composite photocatalyst and that the addition of rGO, even at low concentrations (0.5%), can substantially increase the rate of pollutant degradation compared with GO/TiO_2 and pristine TiO_2. The reduction of GO with hydrogen at higher temperatures led to marked changes in morphological and chemical properties. In terms of morphology, rGO exhibited a much smaller surface area accompanied by the formation of micropores, which is very different from graphene itself. Concerning the chemical properties, such as thermal stability and the content of surface oxygenated groups, they approached those of graphene. The presence of rGO in the composite photocatalyst led to the increased formation of hydroxyl radicals, which explains the enhancement in photocatalytic performance. This mechanism dominated the performance of the composite while the degradation due to the direct charge transfer mechanism was smaller. The present study, together with our previous ones [6,25], form the basis for extensive and complex research into the photocatalytic performance of composites containing different allotropes of TiO_2 and carbonaceous dopants, including fullerene, carbon nanotubes, reduced graphene oxide and graphene itself.

Author Contributions: conceptualization, Jiri Rathousky; methodology, Libor Brabec, Jan Plsek; validation, Jiri Rathousky, Radek Zouzelka, Monika Remzova, Libor Brabec, Jan Plsek; investigation, Monika Remzova, Libor Brabec, Jan Plsek; resources, Jiri Rathousky; data curation, Jiri Rathousky, Radek Zouzelka, Monika Remzova, Libor Brabec, Jan Plsek; writing—original draft preparation, Jiri Rathousky, Radek Zouzelka; writing—review and editing, Jiri Rathousky, Radek Zouzelka; supervision, Jiri Rathousky; project administration, Jiri Rathousky; funding acquisition, Jiri Rathousky.

Funding: This research was funded by the Czech Science Foundation (GACR, Grant No. 19-21801S).

Acknowledgments: This work was supported by the Ministry of Education, Youth and Sports of the Czech Republic and The European Union - European Structural and Investments Funds in the frame of Operational Programme Research, Development and Education - project Pro-NanoEnviCz (Project No.CZ.02.1.01/0.0/0.0/16_013/0001821), which provided an access to the Micromeritics 3Flex apparatus. Finally, the authors thank Craig Riddel (UTC, Prague) for an improvement of the readability of the text.

Conflicts of Interest: The authors declare no conflict of interest. The funders had no role in the design of the study; in the collection, analyses, or interpretation of data; in the writing of the manuscript, or in the decision to publish the results.

References

1. Niu, P.; Zhang, L.; Liu, G.; Cheng, H.M. Graphene-like carbon nitride nanosheets for improved photocatalytic activities. *Adv. Funct. Mater.* **2012**, *22*, 4763–4770.
2. Tu, W.; Zhou, Y.; Zou, Z. Versatile graphene-promoting photocatalytic performance of semiconductors: Basic principles, synthesis, solar energy conversion, and environmental applications. *Adv. Funct. Mater.* **2013**, *23*, 4996–5008.
3. Jeon, S.J.; Kang, T.W.; Ju, J.M.; Kim, M.J.; Park, J.H.; Raza, F.; Han, J.; Lee, H.R.; Kim, J.H. Modulating the Photocatalytic Activity of Graphene Quantum Dots via Atomic Tailoring for Highly Enhanced Photocatalysis under Visible Light. *Adv. Funct. Mater.* **2016**, *26*, 8211–8219.
4. Chabot, V.; Higgins, D.; Yu, A.; Xiao, X.; Chen, Z.; Zhang, J. A review of graphene and graphene oxide sponge: Material synthesis and applications to energy and the environment. *Energy Environ. Sci.* **2014**, *7*, 1564–1596.
5. Li, F.; Jiang, X.; Zhao, J.; Zhang, S. Graphene oxide: A promising nanomaterial for energy and environmental applications. *Nano Energy* **2015**, *16*, 488–515.
6. Guérin, V.-M.; Zouzelka, R.; Bibova-Lipsova, H.; Jirkovsky, J.; Rathousky, J.; Pauporté, T. Experimental and DFT study of the degradation of 4-chlorophenol on hierarchical micro-/nanostructured oxide films. *Appl. Catal. B Environ.* **2015**, *168–169*, 132–140.
7. Li, N.; Liu, G.; Zhen, C.; Li, F.; Zhang, L.; Cheng, H.M. Battery performance and photocatalytic activity of mesoporous anatase TiO2nanospheres/graphene composites by template-free self-assembly. *Adv. Funct. Mater.* **2011**, *21*, 1717–1722.
8. Oishi, I.; Kim, S.; Yoshii, K.; Esteban, C.R.; Izpisua Belmonte, J.C. Cre-LoxP-regulated expression of monoclonal antibodies driven by an ovalbumin promoter in primary oviduct cells. *BMC Biotechnol.* **2011**, *11*, 1–19.
9. A. Dąbrowski Adsorption-from theory to practice. *Adv. Colloid Interface Sci.* **2001**, *93*, 135–224.
10. Zouzelka, R.; Remzova, M.; Brabec, L.; Rathousky, J. Photocatalytic performance of porous TiO<inf>2</inf>layers prepared by quantitative electrophoretic deposition from organic solvents. *Appl. Catal. B Environ.* **2018**, *227*.
11. Liu, J.; Bai, H.; Wang, Y.; Liu, Z.; Zhang, X.; Sun, D.D. Self-assembling TiO_2 nanorods on large graphene oxide sheets at a two-phase interface and their anti-recombination in photocatalytic applications. *Adv. Funct. Mater.* **2010**, *20*, 4175–4181.

12. A.K Geim and K.S. Novoselov The rise of graphene. *Nat. Mater.* **2007**, *183*, 153–160.
13. Shahhriary, L.; Athawale, A.A. Graphene Oxide Synthesized by using Modified Hummers Approach. *Int. J. Renew. Energy Environ. Eng.* **2014**, *02*, 58–63.
14. Rattana, T.; Chaiyakun, S.; Witit-Anun, N.; Nuntawong, N.; Chindaudom, P.; Oaew, S.; Kedkeaw, C.; Limsuwan, P. Preparation and characterization of graphene oxide nanosheets. *Procedia Eng.* **2012**, *32*, 759–764.
15. Li, L.; Yan, J.; Wang, T.; Zhao, Z.-J.; Zhang, J.; Gong, J.; Guan, N. Sub-10 nm rutile titanium dioxide nanoparticles for efficient visible-light-driven photocatalytic hydrogen production. *Nat. Commun.* **2015**, *6*, 5881.
16. Ganguly, A.; Sharma, S.; Papakonstantinou, P.; Hamilton, J. Probing the thermal deoxygenation of graphene oxide using high-resolution in situ X-ray-based spectroscopies. *J. Phys. Chem. C* **2011**, *115*, 17009–17019.
17. Mattevi, C.; Eda, G.; Agnoli, S.; Miller, S.; Mkhoyan, K.A.; Celik, O.; Mastrogiovanni, D.; Granozzi, G.; Carfunkel, E.; Chhowalla, M. Evolution of electrical, chemical, and structural properties of transparent and conducting chemically derived graphene thin films. *Adv. Funct. Mater.* **2009**, *19*, 2577–2583.
18. Akhavan, O. The effect of heat treatment on formation of graphene thin films from graphene oxide nanosheets. *Carbon N. Y.* **2010**, *48*, 509–519.
19. Jeong, H.K.; Yun, P.L.; Lahaye, R.J.W.E.; Park, M.H.; Kay, H.A.; Ick, J.K.; Yang, C.W.; Chong, Y.P.; Ruoff, R.S.; Young, H.L. Evidence of graphitic AB stacking order of graphite oxides. *J. Am. Chem. Soc.* **2008**, *130*, 1362–1366.
20. Yang, D.; Velamakanni, A.; Bozoklu, G.; Park, S.; Stoller, M.; Piner, R.D.; Stankovich, S.; Jung, I.; Field, D.A.; Ventrice, C.A.; et al. Chemical analysis of graphene oxide films after heat and chemical treatments by X-ray photoelectron and Micro-Raman spectroscopy. *Carbon N. Y.* **2009**, *47*, 145–152.
21. Vanquickenborne, L.G.; Vranckx, J.; Görller-walrand, C. On th Kinetic Trans Effect in Square Planar Transition Metal Complexes. *J. Am. Chem. Soc.* **1974**, *96*, 4121–4125.
22. Kubelka, P. New Contributions to the Optics of Intensely Light-Scattering Materials. Part I. *J. Opt. Soc. Am.* **1948**, *38*, 448–457.
23. Ohtani, B. Photocatalysis A to Z-What we know and what we do not know in a scientific sense. *J. Photochem. Photobiol. C Photochem. Rev.* **2010**, *11*, 157–178.
24. TAUC, J. Optical Properties and electronic structure of amorphous. *Mater. Res. Bull.* **1968**, *3*.
25. Hynek, J.; Kalousek, V.; Zouzelka, R.; Bezdicka, P.; Dzik, P.; Rathousky, J.; Demel, J.; Lang, K. High photocatalytic activity of transparent films composed of Zno nanosheets. *Langmuir* **2014**, *30*, 380–386.
26. Motohashi, N; Saito, Y. Competetive measurement of rate constants for hydroxyl radical reactions using radiolytic hydroxylation of benzoate. *Chem. Pharm. Bull. (Tokyo).* **1993**, *41*, 1842–1845.
27. Stafford, U.; Gray, K.A.; Kamat, P. V. Radiolytic and TiO_2-assisted photocatalytic degradation of 4-chlorophenol. A comparative study. *J. Phys. Chem.* **1994**, *98*, 6343–6351.